



This is a repository copy of *Anomalous grain boundary conduction in BiScO₃-BaTiO₃ high temperature dielectrics*.

White Rose Research Online URL for this paper:
<https://eprints.whiterose.ac.uk/177054/>

Version: Accepted Version

Article:

Li, L. orcid.org/0000-0002-9565-9830, Roncal-Herrero, T., Harrington, J. et al. (4 more authors) (2021) Anomalous grain boundary conduction in BiScO₃-BaTiO₃ high temperature dielectrics. *Acta Materialia*, 216. 117136. ISSN 1359-6454

<https://doi.org/10.1016/j.actamat.2021.117136>

© 2021 Acta Materialia Inc. This is an author produced version of a paper subsequently published in *Acta Materialia*. Uploaded in accordance with the publisher's self-archiving policy. Article available under the terms of the CC-BY-NC-ND licence (<https://creativecommons.org/licenses/by-nc-nd/4.0/>).

Reuse

This article is distributed under the terms of the Creative Commons Attribution-NonCommercial-NoDerivs (CC BY-NC-ND) licence. This licence only allows you to download this work and share it with others as long as you credit the authors, but you can't change the article in any way or use it commercially. More information and the full terms of the licence here: <https://creativecommons.org/licenses/>

Takedown

If you consider content in White Rose Research Online to be in breach of UK law, please notify us by emailing eprints@whiterose.ac.uk including the URL of the record and the reason for the withdrawal request.



eprints@whiterose.ac.uk
<https://eprints.whiterose.ac.uk/>

1 Anomalous grain boundary conduction in BiScO₃-BaTiO₃ high temperature 2 dielectrics.

3 Linhao Li^a, Teresa Roncal-Herrero^b, John Harrington^b, Steven J. Milne^b, Andy P. Brown^b, Julian S
4 Dean^a and Derek C Sinclair^{a,*}

5 ^a Department of Materials Science and Engineering, University of Sheffield, Mappin St.,
6 Sheffield, S1 3JD, UK

7 ^b School of Chemical and Process Engineering, University of Leeds, Leeds, LS2 9JT, UK

8 Abstract

9 A combination of X-ray diffraction, analytical-electron microscopy, differential scanning
10 calorimetry, impedance spectroscopy and electromotive force measurements (for oxide-ion
11 transport number measurements, t_{ion}) are used to report on the influence of a small amount of a
12 continuous Bi₂O₃-rich phase along the grain boundaries in sample composition $x = 0.4$ (BS_{0.4}BT) of
13 the high temperature dielectric solid solution series, $x(\text{BiScO}_3)-(1-x)(\text{BaTiO}_3)$. Its presence produces
14 a dramatic change in conductivity of \sim two orders of magnitude and a switch in t_{ion} over the range
15 $\sim 600 - 800$ °C that is not observed for other ceramics with lower BiScO₃ content. Below ~ 700 °C
16 the grain boundaries in BS_{0.4}BT act as electrically blocking layers and dominate the impedance of
17 the ceramics. In contrast, at > 800 °C the grain boundaries become highly conductive due to a
18 polymorphic phase transition to, and melting of δ -Bi₂O₃ which results in the current percolating
19 along the grain boundaries and therefore avoiding the grains. The value of t_{ion} increases from \sim
20 0.13 at ~ 600 °C to near unity at ~ 800 °C for BS_{0.4}BT, consistent with oxide ion conduction due to
21 the presence of liquid Bi₂O₃ at grain boundary regions. This behaviour was reproduced by adding a
22 small excess of 3 wt% Bi₂O₃ into $x = 0.3$ (BS_{0.3}BT) samples to induce a Bi₂O₃-rich grain boundary
23 phase, not otherwise present in this composition.

24 Introduction

25 In recent years there has been significant interest in the development of solid solutions
26 between ferroelectric perovskites such as BaTiO₃ with BiMeO₃ perovskites, e.g. Me = Sc, Ti_{1/2}Mg_{1/2},
27 or Ti_{1/2}Zn_{1/2}, to develop Pb-free temperature stable dielectrics for capacitor applications beyond
28 200 °C.[1–8] These include power electronics, engine communication and management systems in
29 automotives such as electric vehicles and devices operating under harsh environments (e.g. ~ 300
30 – 500 °C). The structure-composition-property relationships in these ABO₃ solid solutions have
31 been intensively studied due to multiple site occupancy on both cation sublattices and segregation

* Corresponding author. E-mail address: d.c.sinclair@sheffield.ac.uk

1 effects on either a micro- and/or nano-scopical scale.[9–17] Such phenomena can influence the
2 short- and long-range order and coupling between the electric dipoles generated via A- and/or B-
3 site displacements in the lattice(s) and therefore impact on the permittivity-temperature (ϵ -T)
4 profiles. With increasing BiMeO₃ content (typically < 10 mol %) there is a cross over from classic
5 ferroelectric behaviour in undoped BaTiO₃ with a very sharp peak in permittivity at the Curie point
6 to a core-shell type response (due to microscopic segregation) that generates a broadened ϵ -T
7 profile with peaks associated with the core and shell regions in the microstructure. At higher
8 BiMeO₃ contents (typically 10 – 40 mol %), the core-shell type ϵ -T profiles (and microstructure) are
9 replaced by highly diffuse and dispersive relaxor type ϵ -T profiles associated with polar nano
10 regions (PNR's). This evolves into relatively temperature-stable ϵ -T profiles (for ~ 20-40 mol%) that
11 exhibit weak relaxor behaviour at lower temperatures (typically < 100 °C) but a high value ϵ -
12 plateau (~ 500 – 1000) between ~ 150 and 500 °C. This makes these materials attractive for the
13 aforementioned high temperature applications.

14 The initial objective of this study was to use Impedance Spectroscopy (IS) to probe the
15 evolution of the grain electrical-microstructure, i.e. the switch from core/shell to NPR's in
16 $x(\text{BiScO}_3)-(1-x)(\text{BaTiO}_3)$ (BS_xBT) with increasing BiScO₃-content, x (which will be addressed in a
17 separate paper). During this study, however, we observed an anomalous high temperature
18 conductivity behaviour for a composition $\text{BS}_{0.4}\text{BT}$ close to the BiScO₃-end of the solid solution limit.
19 This phenomenon is revealed here to be due to a Bi₂O₃ grain boundary phase.

20 Grain boundaries often play a significant role in functional ceramics. In some cases, grain
21 boundary functionality is desired and is central to performance whereas in others their
22 contribution is deleterious and needs to be minimised. Examples of the former are ZnO varistors
23 [18] and positive temperature coefficient resistor (PTCR) BaTiO₃ thermistors [19,20]. Highly
24 resistive grain boundaries are also beneficial in many dielectric ceramics. This is especially
25 important for capacitor applications where dielectric layers are only a few microns in thickness. On
26 the other hand, resistive grain boundaries are undesirable for some applications, such as solid
27 electrolytes for electrochemical devices where there is a drive to minimise the total resistance of
28 the electrolyte.

29 A commonly applied method to study grain and grain boundary impedances in
30 electroceramics is Impedance Spectroscopy, IS. Since the pioneering IS work on Y-stabilised ZrO₂
31 ceramics by Bauerle [21], simple equivalent circuit models based on a Brickwork Layer Model (BLM)
32 approach often work well to extract bulk and grain boundary resistance and capacitance values for
33 micron grain-sized ceramics where the grain boundaries are much more resistive than the grains
34 [22–24]. Data analysis becomes more challenging when the volume fraction of grain boundary
35 regions increases with decreasing grain size (as in nano grain-sized ceramics) and/or the grain
36 boundary regions become more conductive than the grains [25–27]. The generic BLM assumes
37 homogeneous grains (i.e. the bricks) in the form of a 3D array of regular cubes that are encased by
38 homogeneous grain boundaries (i.e. the mortar), Fig 1 (a). A basic equivalent circuit to describe
39 this electrical microstructure contains both series and parallel pathways, i.e. an outer grain
40 boundary pathway that is connected in parallel with a series pathway based on upper and lower

1 grain boundary regions with the grains, Fig 1 (b) (based on an applied voltage across the top and
2 bottom of the sample). In the scenario where the grain boundaries are substantially more resistive
3 than the grains, the equivalent circuit simplifies to only the series pathways with two parallel
4 Resistor-Capacitor networks to represent the grains (or bulk) (R_b, C_b) and the grain boundaries ($R_{gb,s},$
5 $C_{gb,s}$) as there is negligible current via the grain boundaries in parallel pathways. This series model
6 is often referred to as the S-BLM. As the grain boundaries become more conductive the parallel
7 pathways become increasingly important and analysis of the IS data to extract bulk and grain
8 boundary properties becomes challenging. This is often referred to as the series-parallel SP-BLM,
9 i.e. both the series-parallel path in Fig 1 (b). There have been several treatments of this type of
10 scenario as documented elsewhere [25–28].

11 Although Bi-based oxides are commonly investigated for their dielectric properties, [1–8]
12 some are also excellent oxide-ion conducting electrolytes [29–31]. The classic example is Bi_2O_3
13 which exhibits complex polymorphism and hysteresis in the polymorphic transitions [29]. The low
14 temperature α -polymorph is a mixed p-type/oxide ion conductor (predominantly p-type) that
15 transforms on heating to a face centred cubic δ -polymorph at 729 °C that is an excellent oxide-ion
16 conducting electrolyte before melting at ~ 824 °C. There is a three order of magnitude increase in
17 the conductivity associated with the α to δ transition from mS/cm to \sim S/cm and the conductivity
18 of the δ -polymorph is comparable to that of the melt. On cooling, there is significant hysteresis in
19 the δ to α transformation (typically $\sim 80 - 90$ °C) that is dependent on the cooling conditions. The
20 transformation occurs via intermediate polymorphs β and/or γ in the range $\sim 650 - 630$ °C and
21 these subsequently transform to α - Bi_2O_3 from $\sim 650 - 490$ °C. It is possible to stabilise δ - Bi_2O_3 at
22 room temperature by rapid quenching from above the α to δ transition or to lower the transition
23 temperature by chemical doping [30].

24 This script describes the anomalous behaviour observed in $0.4(\text{BiScO}_3)\text{-}0.6(\text{BaTiO}_3)$ that
25 correlates with the presence of Bi_2O_3 -rich grain boundaries. These change from being highly
26 resistive and inter-grain electrically blocking at lower temperatures (< 700 °C) to become
27 percolative and highly (oxide-ion) conductive at high temperatures (> 800 °C). We propose this is
28 linked to a combination of polymorphic phase transition(s) and melting of the Bi_2O_3 -rich grain
29 boundary phase that occurs in the intermediate temperature range ($\sim 700 - 820$ °C). Confirmation
30 of this ‘switch’ from a grain boundary blocking series pathway (S-BLM) to a grain boundary
31 conducting parallel pathway (SP-BLM) was obtained by engineering $0.3(\text{BiScO}_3)\text{-}0.7(\text{BaTiO}_3)$
32 ceramics with and without a Bi_2O_3 -rich grain boundary phase.

33 Experimental procedure

34 Ceramics were prepared by conventional solid-state synthesis: Bi_2O_3 (99.9%, Acros Organics),
35 TiO_2 (99.9%, Sigma-Aldrich), BaCO_3 (99.5%, Sigma-Aldrich) and Sc_2O_3 powders (99.9%, Sigma-
36 Aldrich) were used as raw materials. These were pre-dried for 16 h prior to weighing in appropriate
37 amounts. The batched mixtures were ball milled in isopropanol with yttria-stabilized zirconia (YSZ)
38 milling media for 6 h, dried, sieved and calcined at 800 °C for 2 h in air. The resultant powders were
39 ball milled for 4 h followed by drying, sieving, a 2 h calcination at 850 °C and a further 6 h ball

1 milling. Green pellets were formed by a uniaxial steel die and then isostatically pressed at 200 MPa.
2 These were sintered at 1300 °C for 2 h in air. All pellets were covered in calcined powder of the
3 same composition to minimise volatilisation during sintering.

4 X-ray powder diffraction (XRD) analysis was performed on sintered and crushed samples using
5 a high-resolution STOE STADI-P diffractometer (Cu K α radiation). Microstructure and compositional
6 analysis were determined by a combination of a Philips XL 30S FEG scanning electron microscope
7 with a Noran energy dispersive X-ray analyser and subsequent TEM (described below). Ceramic
8 samples for SEM were polished or polished and thermally etched at 1170 °C for 1 h before being
9 coated with carbon. The melting and solidification process of a Bi₂O₃ phase was monitored with
10 differential scanning calorimetry (DSC) using a Netzsch DSC 404 C thermal analyser on sintered and
11 crushed samples. The DSC experiments were performed under flowing air from 20 to 900 °C at
12 heating/cooling rates of 5 °C/min.

13 Samples were prepared for transmission electron microscopy (TEM) following two routes. In
14 the first route a sintered pellet was crushed to a fine powder using an agate pestle and mortar: the
15 powder was then dispersed in ethanol, sonicated for 2 minutes in an ultrasonic bath and drop-cast
16 onto a holey carbon film supported on 400 mesh copper finder grids (EM resolution Ltd). In the
17 second route, a thin lamella was prepared using a Focused Ion Beam FEI Helios G4 CX Dual Beam
18 microscope with in-situ-lift out onto dedicated support grids for TEM (Omniprobe Inc). Here, a final
19 ion beam clean was performed at 5 kV and 40 pA to reduce any side-wall damage to the section.
20 The nominal thickness of the lamella was ~50 nm, as measured by SEM imaging. All samples were
21 analysed on a FEI Titan Themis³ G2 transmission electron microscope operated at 300 kV, with a
22 monochromator and a Super-X 4-detector silicon drift energy dispersive X-ray (EDX) system. High
23 angle annular dark field (HAADF) images were collected over the scattering semi-angle range of
24 35-150 mrad. STEM was run with a 1.4 Å probe diameter of 10 mrad convergence semi angle; probe
25 currents were varied by the monochromator (not excited) and ranged from 40 – 200 pA depending
26 on the imaging and mapping mode. EDX spectra were processed in Velox 2.1 and elemental
27 quantification undertaken using the standard-less method within the software, involving
28 estimation of thickness, density and fitting of Brown-Powell cross-sections with a +/- 2 eV
29 uncertainty.

30 Impedance spectroscopy was performed on sintered ceramics coated with Au-paste
31 electrodes using a Solartron Modulab and a Hewlett Packard 4284A Precision LCR meter. The data
32 were corrected for sample geometry (thickness/area). Oxygen ion transport number was taken via
33 electromotive force (EMF) method on a ProboStat system at 600–800 °C. A gas concentration cell
34 was prepared using N₂ and air to generate an oxygen partial pressure (pO₂) gradient. A YSZ tube
35 was used as a pO₂ monitor as described previously [32].

36 In the following text, sample compositions x(BiScO₃)-(1-x)(BaTiO₃) are labelled as BS_xBT, where
37 x represents the mole fraction of BiScO₃, x = 0.2, 0.3 and 0.4. The 0.3(BiScO₃)-0.7(BaTiO₃) + 3wt%
38 Bi₂O₃ samples are labelled as BS_{0.3}BT-Bi.

1 Results

2 The XRD patterns of BS_xBT ceramics for $x = 0.2-0.4$ are displayed in Fig 2 (a). Diffraction
3 patterns could be fully indexed using a cubic cell (space group Pm-3m) for all samples except for
4 $BS_{0.4}BT$ where an additional low intensity peak at $28.3^\circ 2\theta$ indicates the presence of $\beta-Bi_2O_3$ (ICSD:
5 62979) as a secondary phase. Rietveld analysis shows the amount of Bi_2O_3 is about 1.2 wt%, Fig S1.
6 A small increase in lattice parameter was observed with increasing $BiScO_3$ (BS) content, Fig 2 (b).
7 The density is relatively low for $BS_{0.2}BT$ (84%) ceramics due to the sintering temperature used but
8 it significantly improved for $BS_{0.3}BT$ and $BS_{0.4}BT$ (reaching >94%), Fig 2 (b).

9 SEM images of thermally etched BS_xBT ceramics are shown in Fig 3 (a-c). The grain size is
10 between 2-5 μm in $BS_{0.2}BT$ and 5-10 μm in $BS_{0.3}BT$ and $BS_{0.4}BT$. The presence of a Bi_2O_3 phase in
11 $BS_{0.4}BT$ was further confirmed by a combination of SEM/EDX and TEM with an additional Sc_2O_3
12 phase also being detected by SEM, Fig 3 (f) and (g). The Bi_2O_3 and Sc_2O_3 phases are mainly
13 accumulated at grain boundary triple pockets as these are identified to be Bi, Sc and O rich by EDX,
14 Fig 3 (f). TEM images show these islands are connected via very thin (<2 nm) layers rich in Bi and O
15 along grain boundaries, Fig 3 (g). Samples of $BS_{0.3}BT$ appeared phase pure by SEM and TEM with
16 no evidence of Bi and O enrichment along the grain boundaries, Fig 3 (d) and (e), which agrees
17 with the XRD results in Fig 2 (a).

18 The DSC data on $BS_{0.4}BT$ showed clear evidence of an endothermic process occurring on
19 heating with an onset temperature of $\sim 818^\circ C$ and an exothermic process with an onset
20 temperature of $\sim 799^\circ C$ on cooling, Fig. 4. There were no DSC thermal events observed on
21 heating/cooling for $BS_{0.2}BT$ over the same temperature range and although no clear DSC peaks
22 were observed for $BS_{0.3}BT$ there were significant changes in the baseline slope at $\sim 818^\circ C$ and \sim
23 $799^\circ C$ on the heating and cooling cycles, respectively, Fig 4.

24 The temperature dependent relative permittivity (ϵ_r) and dielectric loss tangent ($\tan \delta$) at
25 1MHz from room temperature to $\sim 850^\circ C$ are shown in Fig 5. A broad, relatively temperature-
26 insensitive permittivity response is observed in all three BS-BT ceramics. The maximum permittivity
27 (ϵ_{max}) increases from ~ 850 for $BS_{0.2}BT$ to ~ 1100 for $BS_{0.4}BT$. The value of $\tan \delta$ of all three samples
28 is low (< 0.02) within the temperature range 200 – 400 $^\circ C$. At higher temperatures (> 400 $^\circ C$), both
29 the ϵ_r and $\tan \delta$ values of $BS_{0.4}BT$ show hysteresis behaviour on heating and cooling, which was not
30 observed for $BS_{0.2}BT$ and $BS_{0.3}BT$.

31 The EMF method was used to measure the oxygen-ion transport number (t_{ion}) of the ceramics
32 in the range of ~ 600 to 900 $^\circ C$, Fig 6 (c) & (d). The value of t_{ion} was negligible for $BS_{0.2}BT$ (~ 0.02)
33 indicating the ceramics were predominantly electronically conducting over this temperature range
34 whereas $BS_{0.3}BT$ ceramics gave $t_{ion} \sim 0.17$ indicating mixed ionic-electronic conduction. In contrast,
35 t_{ion} of $BS_{0.4}BT$ was very temperature dependent. The value was low (< 0.25) at temperatures < 650
36 $^\circ C$ but increased rapidly above 700 $^\circ C$ and approached unity at temperatures $\geq 800^\circ C$, Fig 6 (d).
37 This indicates mixed ionic-electronic conduction at $\sim 650^\circ C$ which is replaced by oxide-ion
38 conduction in $BS_{0.4}BT$ ceramics at $\sim 800^\circ C$. It is noteworthy that the rapid change in t_{ion} with

1 temperature occurs over the same temperature range as the hysteresis in the ϵ_r data, Fig 5. To
2 investigate the electrical properties in more detail, IS was performed on all of these ceramics. The
3 aim was not to fully fit the data using equivalent circuit analysis but rather to assess the total
4 conductivity (σ_T) of the BS_x BT ceramics based on inspection of Z^* plots and to identify the presence
5 and/or absence of electronic and/or ionic conduction. This involved: (i) identifying (where possible)
6 bulk and grain boundary responses by the presence of high and intermediate frequency Z^* arcs
7 with appropriate associated capacitance values [33]; (ii) identifying ionic or mixed ionic-electronic
8 conduction via the presence and/or absence of a finite or infinite Warburg response respectively
9 at low frequencies in the Z^* plots [34]; (iii) taking σ_T as the reciprocal of the low frequency intercept
10 on the real axis of Z^* plots between the ceramic and electrode responses (preceding points (i) and
11 (ii), respectively).

12 The Z^* response for $BS_{0.2}$ BT at 600 °C consisted of a single, large arc with an associated
13 capacitance of ~ 37 pF/cm and little evidence of any significant low frequency electrode response
14 associated with mixed conduction, Fig 6 (a) and Fig S1 (a). The Z^* response at 900 °C consists of a
15 partial arc, Fig 6 (b); however, closer inspection of the low frequency data indicated the presence
16 of a very small electrode effect that was difficult to resolve and could not be investigated in detail,
17 Fig 6 (b) and Fig S1(b). The impedance data for $BS_{0.2}$ BT are consistent with σ_T being a bulk-type
18 response. The absence of any significant electrode effects in Z^* , in combination with the negligible
19 t_{ion} values, indicate the bulk conduction to be electronic. An Arrhenius plot of σ_T for $BS_{0.2}$ BT gives a
20 linear response with an activation energy (E_a) for the bulk conduction of ~ 1.22 eV.

21 The Z^* response for $BS_{0.3}$ BT at 600 °C was significantly different to that observed for $BS_{0.2}$ BT.
22 At 600 °C the data show clear evidence of two poorly resolved large arcs in Z^* , Fig 6 (a), with
23 evidence on closer inspection of a third, much smaller but significantly broadened arc response at
24 lower frequencies, Fig S1 (c). The high frequency arc in Z^* has an associated capacitance of ~ 40
25 pF/cm which is similar in magnitude to that observed for $BS_{0.2}$ BT at the same temperature, Fig 6 (a)
26 and is therefore attributed to a bulk response. The additional large arc at lower frequencies for
27 $BS_{0.3}$ BT has an associated capacitance of ~ 150 pF/cm and is attributed to a grain boundary
28 response, Fig 6 (a). As a consequence of the grain boundary impedance, σ_T is about a factor of two
29 lower for $BS_{0.3}$ BT when compared to $BS_{0.2}$ BT at 600 °C. The third arc at lower frequency has an
30 associated capacitance of ~ 25 nF/cm and is attributed to an electrode effect associated with
31 diffusion of oxide ions at the ceramic/electrode interface, Fig S1(c). The Z^* response at 900 °C for
32 $BS_{0.3}$ BT also shows a partial arc, Fig 6 (b) that is associated with the response from the ceramic and
33 clear evidence of the ceramic/electrode interface Z^* response at lower frequency. The impedance
34 data for $BS_{0.3}$ BT ceramics are therefore consistent with σ_T being a combined bulk and grain
35 boundary type response. The presence of the electrode effects in Z^* in combination with $t_{ion} \sim 0.17$
36 confirms the conduction behaviour in the ceramics to be mixed ionic-electronic conduction. An
37 Arrhenius plot of σ_T for $BS_{0.3}$ BT gives a very similar trend and E_a value to that obtained for $BS_{0.2}$ BT,
38 Fig 6 (c), indicating that bulk conduction dominates σ_T over the measured range from 600 -900 °C.

39 For $BS_{0.4}$ BT there was a large asymmetric arc that was at least one order of magnitude greater
40 at 600 °C compared with $BS_{0.2}$ BT or $BS_{0.3}$ BT. In this case, it was not possible to resolve or identify

1 bulk or grain boundary components from Z^* plots and this response was attributed to the overall
2 ceramic such that σ_T at 600 °C was significantly lower for $BS_{0.4}BT$ compared to $BS_{0.2}BT$ and $BS_{0.3}BT$.
3 Closer inspection of the low frequency data in the Z^* plot did not indicate the presence of a
4 significant response associated with a ceramic/electrode interface effect, Fig S1 (d); however, this
5 could have been masked by the large impedance response associated with the ceramic at 600 °C.
6 In contrast, the Z^* response for $BS_{0.4}BT$ at 900 °C had the lowest impedance of all the BS-BT
7 ceramics, Fig 6 (b), with the response being dominated by a low frequency spike associated with
8 Warburg diffusion ($\sim 450 \mu F/cm$) indicating the presence of ionic conduction. An Arrhenius plot of
9 σ_T for $BS_{0.4}BT$ showed anomalous behaviour that could be subdivided into three regions with E_a
10 values of ~ 1.84 eV (<750 °C), 5.43 eV (~ 750 - 875 °C) and 0.58 eV (>875 °C). It is noteworthy that
11 all E_a values are very different to those obtained for $BS_{0.2}BT$ and $BS_{0.3}BT$ (~ 1.22 eV). Combining the
12 impedance data with the variation in t_{ion} from ~ 0.25 at 600 °C to near unity at $> \sim 775$ °C, shows
13 $BS_{0.4}BT$ ceramics exhibit mixed ionic-electronic conduction at 600 °C but are ionically conducting
14 above ~ 800 °C. Given the clear evidence for a Bi_2O_3 -rich grain boundary phase in $BS_{0.4}BT$ from the
15 electron microscopy, Figs 2 and 3, and its absence in $BS_{0.2}BT$ and $BS_{0.3}BT$, we prepared a new batch
16 of $BS_{0.3}BT$ with an additional 3wt.% Bi_2O_3 in the starting composition, i.e. $BS_{0.3}BT-Bi$. The aim being
17 to induce a Bi_2O_3 -rich grain boundary phase and to use this to assess the influence of the grain
18 boundary modification on the electrical properties.

19 The XRD data for $BS_{0.3}BT$ and $BS_{0.3}BT-Bi$ show no evidence of any additional reflections
20 associated with the excess Bi sample, $BS_{0.3}BT-Bi$, Fig 7 (a). This result for $BS_{0.3}BT-Bi$ is in contrast to
21 $BS_{0.4}BT$ where the presence of β - Bi_2O_3 was visible by XRD, Fig 2(a). There is a small decrease in the
22 lattice parameter and a modest increase in the density of the ceramics for $BS_{0.3}BT-Bi$ compared to
23 $BS_{0.3}BT$, inset Fig 7 (a). The grain sizes of $BS_{0.3}BT-Bi$ were in the range of 7-15 μm which are slightly
24 larger compared to $BS_{0.3}BT$, Fig 7 (b). The SEM back-scattering images revealed bright regions of
25 contrast associated with a secondary phase in $BS_{0.3}BT-Bi$ and EDX confirmed this to be Bi and O rich
26 i.e. Bi_2O_3 , Fig 7 (c). Furthermore, TEM revealed clear Bi-enrichment in triple pockets areas and
27 along the grain boundaries in $BS_{0.3}BT-Bi$, Fig 7 (c). These results confirm the presence of a Bi-rich
28 grain boundary phase in $BS_{0.3}BT-Bi$ ceramics that is similar to that observed for $BS_{0.4}BT$, Fig 3 (f) and
29 (g). The inability of XRD to detect Bi_2O_3 in $BS_{0.3}BT-Bi$ compared to $BS_{0.4}BT$ is therefore attributed to
30 either a lower amount of this phase or it being amorphous in $BS_{0.3}BT$ ceramics. The DSC data
31 revealed exothermic and endothermic processes for $BS_{0.3}BT-Bi$ on heating and cooling, respectively
32 at the same temperatures as those observed for $BS_{0.4}BT$, Fig 4. The DSC peaks are less pronounced
33 for $BS_{0.3}BT-Bi$ compared to $BS_{0.4}BT$ which is consistent with a lower level and/or amorphous Bi_2O_3
34 being present in $BS_{0.3}BT$ and is also consistent with the XRD data in Fig 2 (a) and Fig 7 (a).

35 The dielectric properties of $BS_{0.3}BT$ and $BS_{0.3}BT-Bi$ are broadly in agreement over the
36 temperature range from RT to ~ 600 °C, Fig 8; however, there are significant deviations above 600
37 °C for $BS_{0.3}BT-Bi$. The ϵ_r data show an anomalous dip commencing at ~ 700 °C and both ϵ_r and \tan
38 δ display hysteresis on heating and cooling in this high temperature range, Fig 8. The Z^* plots for
39 $BS_{0.3}BT-Bi$ at 600 °C and 900 °C are shown in Figs. 8 (a) and (b), respectively. In contrast to $BS_{0.3}BT$,
40 where bulk and grain boundary responses can be resolved, only a large and asymmetric arc is
41 present in $BS_{0.3}BT-Bi$ at 600 °C with σ_T being at least a factor of two lower for $BS_{0.3}BT-Bi$, Fig 8 (a).

1 In contrast, Z^* plots for 900 °C show $BS_{0.3}BT-Bi$ to be less resistive than $BS_{0.3}BT$ with the presence
2 of a low angle spike at low frequencies, inset Fig 9 (b). The Arrhenius plot of σ_T for $BS_{0.3}BT-Bi$ in Fig
3 9 (c), reveals similar anomalous behaviour to that observed for $BS_{0.4}BT$ and can be subdivided into
4 three regions based on changes in E_a . Although the values of E_a are different, the trend is the same
5 in $BS_{0.3}BT-Bi$ and $BS_{0.4}BT$, i.e. in the former E_a changes from ~ 1.88 eV (< 750 °C) to ~ 3.55 eV (750-
6 850 °C) and eventually ~ 0.31 eV (> 850 °C) on heating and in the latter E_a changes from ~ 1.84 eV
7 (< 750 °C) to 5.43 eV ($\sim 750-875$ °C) and finishes at 0.58 eV (> 875 °C). The t_{ion} of $BS_{0.3}BT-Bi$ also
8 increases rapidly with increasing temperature and reaches > 0.96 at temperatures > 800 °C, Fig 9
9 (d). This confirms a switch from mixed ionic-electronic conduction at ~ 600 °C to predominantly
10 oxide-ion conduction at ~ 800 °C, Fig 9 (c) and (d). In summary, the anomalous high temperature
11 conduction properties observed for $BS_{0.4}BT$ and the exothermic and endothermic events observed
12 in DSC data were successfully reproduced by adding a small excess of Bi_2O_3 into $BS_{0.3}BT$. This
13 indicates the high σ_T and t_{ion} at high temperature, the change of E_a with temperature and the
14 hysteresis behaviour of ϵ_r and $\tan \delta$ in $BS_{0.4}BT$ are associated with the presence of the Bi_2O_3
15 secondary phase located in the triple points and along grain boundaries in the ceramics.

16 Discussion

17 As the $BiScO_3$ content increases within the series of ceramics $x(BiScO_3)-(1-x)(BaTiO_3)$ (without
18 the addition of any excess Bi_2O_3) the influence of the grain boundary regions on σ_T and t_{ion} become
19 increasingly important. Based on the XRD and SEM/TEM data, Figs 2 and 3, the BS_xBT solid solution
20 limit is between $x \sim 0.3$ ($BS_{0.3}BT$) and 0.4 ($BS_{0.4}BT$). This is in reasonable agreement with that
21 reported previously for $BS-BT$ ceramics [3] and our data show that beyond the solid solution limit,
22 Bi_2O_3 (and to a lesser extent Sc_2O_3) reside in triple points and grain boundary regions. For $BS_{0.4}BT$
23 there is sufficient excess Bi_2O_3 to form a continuous (or a near continuous) network along the grain
24 boundaries and at the triple points, Fig 3 (f) and (g). Because σ_T and E_a of $BS_{0.2}BT$ and $BS_{0.3}BT$ are
25 relatively similar (more so for their bulk conductivity) and since the solid solution limit is at $x \sim 0.3$,
26 it is reasonable to expect that the bulk conductivity of $BS_{0.4}BT$ should be similar to $BS_{0.2}BT$ and
27 $BS_{0.3}BT$. Therefore, we propose that these Bi_2O_3 -rich grain boundary regions are resistive at lower
28 temperatures (e.g. < 600 °C) and dominate the Z^* response, Fig 6 (a) inset, and σ_T of the ceramics,
29 Fig 6 (c). This would suggest an equivalent circuit (to a first approximation) based on a series
30 pathway in Fig 1 (b) is the most appropriate model to start any detailed studies on trying to
31 deconvolute σ_T into bulk and grain boundary components. The dramatic increase in t_{ion} from ~ 0.25
32 to near unity in the range ~ 675 °C to 775 °C suggests transformation to the oxide-ion conducting
33 $\delta-Bi_2O_3$ polymorph is occurring. This transition was not observed by DSC; however, melting of the
34 Bi_2O_3 -rich phase was observed and occurs at ~ 820 °C, Fig 4. Therefore, we attribute the switch
35 over in σ_T in the Arrhenius plot for $BS_{0.4}BT$ ceramics in the range $\sim 750 - 875$ °C with $E_a \sim 5.5$ eV to
36 be associated with polymorphic and state of matter (solid to liquid) changes in the Bi_2O_3 -rich grain
37 boundary regions.

38 Above 850 °C the most appropriate equivalent circuit to analyse IS data would be based (to a
39 first approximation) on a single parallel $R_{gb,p}C_b$ element connected in series with a Warburg

1 element. This would reflect the physical situation of the permittivity associated with the grains (C_b)
2 combined with the short-circuiting, parallel pathway ($R_{gb,p}$, see Fig 1 (b)) associated with a highly
3 oxide ion conducting liquid Bi_2O_3 network along the grain boundaries. Proposing an equivalent
4 circuit, or plausible equivalent circuits, for the intermediate temperature region is beyond the
5 scope of the present work but would require the use of both parallel and series conduction
6 pathways, Fig 1 (b).

7 In contrast, $\text{BS}_{0.2}\text{BT}$ ceramics show only a bulk response in Z^* plots, Fig 6 (a) with no evidence
8 of a grain boundary phase by electron microscopy or any phase transitions in DSC, Fig 4. Linear
9 Arrhenius-type behaviour is observed for σ_T , Fig 6 (c) and when combined with the negligible t_{ion}
10 across the measured temperature range indicates $\text{BS}_{0.2}\text{BT}$ is electronically insulating with $E_a \sim 1.22$
11 eV. This behaviour is consistent with the expected dielectric behaviour for stoichiometric BS_xBT
12 ceramics.

13 The case of $\text{BS}_{0.3}\text{BT}$ is interesting. A grain boundary response is apparent in Z^* at 600°C but it
14 doesn't dominate σ_T or cause a switch in σ_T at higher temperatures, Fig 6. However, the transport
15 number is significantly higher compared to $\text{BS}_{0.2}\text{BT}$ and there is a change in baseline slope but no
16 clear peaks in the DSC at high temperatures, Fig 4. This suggests some Bi_2O_3 -rich grain boundaries
17 are present but that they never form an interconnected liquid network at higher temperatures to
18 cause a sufficient parallel conducting network that allows by-passing of the grain (electronic)
19 response. This would explain why switching of σ_T is not observed. Additional support for this
20 hypothesis is that σ_T and the associated E_a for $\text{BS}_{0.3}\text{BT}$ is very similar to $\text{BS}_{0.2}\text{BT}$, Fig 6 (c). If a grain
21 response was responsible for the t_{ion} , then a change in σ_T and E_a for these two compositions would
22 be expected, but is not observed.

23 The combined DSC, SEM/TEM, IS and t_{ion} data for $\text{BS}_{0.3}\text{BT-Bi}$ (Bi-excess) ceramics clearly
24 support the proposal that the switch in conduction type and level of conductivity is associated with
25 the presence of a Bi_2O_3 -rich grain boundary phase which melts at $\sim 820^\circ\text{C}$, figures 4, 7 and 9,
26 respectively. The hysteresis between ~ 600 and 800°C in the 1 MHz ϵ_r and $\tan \delta$ data on heating
27 and cooling in $\text{BS}_{0.4}\text{BT}$ and $\text{BS}_{0.3}\text{BT-Bi}$ also support this hypothesis, Figs 5 and 8, respectively. It is
28 important to stress that this unusual electrical behaviour is a high temperature phenomenon and
29 doesn't influence the ϵ_r and $\tan \delta$ properties of BS_xBT ceramics at temperatures of $< 400^\circ\text{C}$ where
30 they are being considered for capacitor applications. In fact, σ_T of $\text{BS}_{0.4}\text{BT}$ and $\text{BS}_{0.3}\text{BT-Bi}$ below 400°C
31 is lower than $\text{BS}_{0.2}\text{BT}$ and $\text{BS}_{0.3}\text{BT}$, Fig 6 (c) and 9, and is therefore beneficial for their low field
32 insulation resistance and possibly their breakdown strength depending on how the electric field is
33 distributed in these ceramics.

34 Bismuth oxide grain boundary wetting that gives rise to enhanced ionic diffusion and conductivity
35 has been reported previously. For example, $\text{Bi}_2\text{CuO}_4\text{-Bi}_2\text{O}_3$ composite ceramics show similar
36 anomalous rises in high temperature transport properties (occurring at ~ 730 and 770°C) that are
37 attributed to the α - to δ -polymorphic transition and melting of Bi_2O_3 at the grain boundaries,
38 respectively, and result in parallel conduction pathways throughout the ceramics [35]. It is
39 noteworthy that anomalous jumps in electrical conductivity at $\sim 770^\circ\text{C}$ have recently been
40 reported for Sr-doped BiFeO_3 ceramics [36]. In this case, the behaviour was attributed to a bulk-

1 related phenomenon as opposed to a grain boundary effect. No information was provided as to
2 whether or not there was Bi₂O₃ segregation at the grain boundaries in those ceramics and this may
3 merit further investigation.

4 The phenomenon we describe here may be common in Bi-based oxides processed by solid
5 state reactions because of the volatility and low melting point of Bi₂O₃ as a starting reagent. To
6 suppress and/or compensate for this volatilisation, it is common practice to either add a small
7 excess of Bi₂O₃ to the nominal starting stoichiometry [3] and/or to cover pellets with sacrificial
8 powder prior to sintering of ceramics [31]. However Bi₂O₃ can also act as a sintering aid and
9 therefore assist with densification of ceramics [33].

10 In conclusion, we highlight a potential grain boundary conduction issue surrounding
11 functional ceramics based on Bi-based oxides such as BS_xBT, or where Bi₂O₃ is added as a sintering
12 aid. If excess Bi₂O₃ is present as a secondary phase and is distributed along grain boundaries then
13 high temperature polymorphic phase transitions and melting (at ~ 820 °C) can induce high levels
14 of oxide-ion conductivity that can significantly influence the high temperature electrical properties.

15 Acknowledgments

16 We thank the EPSRC for funding Analysis of Polar Nanostructures in High Temperature Relaxor
17 Dielectrics: A Framework for Materials Discovery (EP/P015514/1 and EP/P015565/1).

18 References

- 19 [1] C.C. Huang, D.P. Cann, X. Tan, N. Vittayakorn, Phase transitions and ferroelectric properties in
20 BiScO₃-Bi(Zn_{1/2}Ti_{1/2})O₃-BaTiO₃ solid solutions, *J. Appl. Phys.* 102 (2007) 044103.
21 <https://doi.org/10.1063/1.2769787>.
- 22 [2] C.C. Huang, D.P. Cann, Phase transitions and dielectric properties in Bi(Zn_{1/2}Ti_{1/2})O₃ -BaTiO₃
23 perovskite solid solutions, *J. Appl. Phys.* 104 (2008) 024117. <https://doi.org/10.1063/1.2960469>.
- 24 [3] H. Ogihara, C.A. Randall, S. Trolier-McKinstry, Weakly coupled relaxor behavior of BaTiO₃-BiScO₃
25 ceramics, *J. Am. Ceram. Soc.* 92 (2009) 110–118. [https://doi.org/10.1111/j.1551-](https://doi.org/10.1111/j.1551-2916.2008.02798.x)
26 [2916.2008.02798.x](https://doi.org/10.1111/j.1551-2916.2008.02798.x).
- 27 [4] Q. Zhang, Z. Li, F. Li, Z. Xu, Structural and Dielectric Properties of Bi (Mg_{1/2}Ti_{1.2})O₃ -BaTiO₃ Lead-
28 Free Ceramics, *J. Am. Ceram. Soc.* 94 (2011) 4335–4339. [https://doi.org/10.1111/j.1551-](https://doi.org/10.1111/j.1551-2916.2011.04695.x)
29 [2916.2011.04695.x](https://doi.org/10.1111/j.1551-2916.2011.04695.x).
- 30 [5] A. Zeb, S.J. Milne, Dielectric and Piezoelectric Properties of (1-x)K_{0.5}Bi_{0.5}TiO₃ - x Ba(Ti_{0.8}Zr_{0.2})O₃
31 Ceramics, *J. Am. Ceram. Soc.* 96 (2013) 3089–3093. <https://doi.org/10.1111/jace.12425>.
- 32 [6] A. Zeb, S.J. Milne, Stability of High-Temperature Dielectric Properties for (1-x)Ba_{0.8}Ca_{0.2}TiO₃ - x

- 1 Bi(Mg_{0.5}Ti_{0.5})O₃ Ceramics, J. Am. Ceram. Soc. 96 (2013) 2887–2892.
2 <https://doi.org/10.1111/jace.12412>.
- 3 [7] A. Zeb, Y. Bai, T. Button, S.J. Milne, Temperature-Stable Relative Permittivity from –70°C to 500°C
4 in (Ba_{0.8}Ca_{0.2})TiO₃ - Bi(Mg_{0.5}Ti_{0.5})O₃ -NaNbO₃ Ceramics, J. Am. Ceram. Soc. 97 (2014) 2479–2483.
5 <https://doi.org/10.1111/jace.12949>.
- 6 [8] A. Zeb, S.J. Milne, High temperature dielectric ceramics: a review of temperature-stable high-
7 permittivity perovskites, J. Mater. Sci. Mater. Electron. 26 (2015) 9243–9255.
8 <https://doi.org/10.1007/s10854-015-3707-7>.
- 9 [9] D.S. Tinberg, S. Trolier-Mckinstry, Structural and electrical characterization of xBiScO₃-(1-x)
10 BaTiO₃ thin films, J. Appl. Phys. 101 (2007) 024112. <https://doi.org/10.1063/1.2430627>.
- 11 [10] S. Trolier-Mckinstry, M.D. Biegalski, J. Wang, A.A. Belik, E. Takayama-Muromachi, I. Levin,
12 Growth, crystal structure, and properties of epitaxial BiScO₃ thin films, J. Appl. Phys. 104 (2008)
13 044102. <https://doi.org/10.1063/1.2964087>.
- 14 [11] K. Datta, P.A. Thomas, Structural investigation of a novel perovskite-based lead-free ceramics:
15 XBiScO₃ -(1-x)BaTiO₃, J. Appl. Phys. 107 (2010) 043516. <https://doi.org/10.1063/1.3309064>.
- 16 [12] S.S.N. Bharadwaja, J.R. Kim, H. Ogihara, L.E. Cross, S. Trolier-McKinstry, C.A. Randall, Critical
17 slowing down mechanism and reentrant dipole glass phenomena in (1-x)BaTiO₃xBiScO₃
18 (0.1≤x≤0.4): The high energy density dielectrics, Phys. Rev. B. 83 (2011) 024106.
19 <https://doi.org/10.1103/PhysRevB.83.024106>.
- 20 [13] H. Takenaka, I. Grinberg, S. Liu, A.M. Rappe, Slush-like polar structures in single-crystal relaxors,
21 Nature. 546 (2017) 391–395. <https://doi.org/10.1038/nature22068>.
- 22 [14] V. Krayzman, I. Levin, J.C. Woicik, F. Bridges, Correlated rattling-ion origins of dielectric
23 properties in reentrant dipole glasses BaTiO₃ -BiScO₃, Appl. Phys. Lett. 107 (2015) 192903.
24 <https://doi.org/10.1063/1.4935417>.
- 25 [15] I. Levin, V. Krayzman, J.C. Woicik, F. Bridges, G.E. Sterbinsky, T.M. Usher, J.L. Jones, D. Torrejon,
26 Local structure in BaTiO₃ -BiScO₃ dipole glasses, Phys. Rev. B. 93 (2016) 104106.
27 <https://doi.org/10.1103/PhysRevB.93.104106>.
- 28 [16] T.M. Usher, T. Iamsasri, J.S. Forrester, N. Raengthon, N. Triamnak, D.P. Cann, J.L. Jones, Local and
29 average structures of BaTiO₃ - Bi(Zn_{1/2}Ti_{1/2})O₃, J. Appl. Phys. 120 (2016) 184102.
30 <https://doi.org/10.1063/1.4967222>.
- 31 [17] T. Roncal-Herrero, J. Harrington, A. Zeb, S.J. Milne, A.P. Brown, Nanoscale compositional
32 segregation and suppression of polar coupling in a relaxor ferroelectric, Acta Mater. 158 (2018)
33 422–429. <https://doi.org/10.1016/j.actamat.2018.07.053>.

- 1 [18] L.M. Levinson, H.R. Philipp, Zinc oxide varistors—a review, *Am. Ceram. Soc. Bull.* 65 (1986) 639–
2 646.
- 3 [19] W. Heywang, Bariumtitanat als sperrschichtableiter, *Solid State Electron.* 3 (1961) 51–58.
4 [https://doi.org/10.1016/0038-1101\(61\)90080-6](https://doi.org/10.1016/0038-1101(61)90080-6).
- 5 [20] G.H. Jonker, Some aspects of semiconducting barium titanate, *Solid State Electron.* 7 (1964)
6 895–903. [https://doi.org/10.1016/0038-1101\(64\)90068-1](https://doi.org/10.1016/0038-1101(64)90068-1).
- 7 [21] J.E. Bauerle, Study of solid electrolyte polarization by a complex admittance method, *J. Phys.*
8 *Chem. Solids.* 30 (1969) 2657–2670. [https://doi.org/10.1016/0022-3697\(69\)90039-0](https://doi.org/10.1016/0022-3697(69)90039-0).
- 9 [22] N.M. Beekmans, L. Heyne, Correlation between impedance, microstructure and composition of
10 calcia-stabilized zirconia, *Electrochim. Acta.* 21 (1976) 303–310. [https://doi.org/10.1016/0013-4686\(76\)80024-2](https://doi.org/10.1016/0013-4686(76)80024-2).
11
- 12 [23] T. van Dijk, A.J. Burggraaf, Grain boundary effects on ionic conductivity in ceramic $Gd_xZr_{1-x}O_{2-(x/2)}$
13 solid solutions, *Phys. Status Solidi.* 63 (1981) 229–240.
14 <https://doi.org/10.1002/pssa.2210630131>.
- 15 [24] M. VERKERK, B. MIDDELHUIS, A. BURGGRAAF, Effect of grain boundaries on the conductivity of
16 high-purity $ZrO_2\text{-}Y_2O_3$ ceramics, *Solid State Ion.* 6 (1982) 159–170.
17 [https://doi.org/10.1016/0167-2738\(82\)90083-2](https://doi.org/10.1016/0167-2738(82)90083-2).
- 18 [25] H. Näfe, Ionic conductivity of ThO_2 - and ZrO_2 -based electrolytes between 300 and 2000 K, *Solid*
19 *State Ion.* 13 (1984) 255–263. [https://doi.org/10.1016/0167-2738\(84\)90040-7](https://doi.org/10.1016/0167-2738(84)90040-7).
- 20 [26] J. Fleig, J. Maier, A Finite Element Study on the Grain Boundary Impedance of Different
21 Microstructures, *J. Electrochem. Soc.* 145 (1998) 2081–2089.
22 <https://doi.org/10.1149/1.1838600>.
- 23 [27] N.J. Kidner, N.H. Perry, T.O. Mason, E.J. Garboczi, The Brick Layer Model Revisited: Introducing
24 the Nano-Grain Composite Model, *J. Am. Ceram. Soc.* 91 (2008) 1733–1746.
25 <https://doi.org/10.1111/j.1551-2916.2008.02445.x>.
- 26 [28] J.P. Heath, J.H. Harding, D.C. Sinclair, J.S. Dean, The Analysis of Impedance Spectra for Core–Shell
27 Microstructures: Why a Multiformalism Approach is Essential, *Adv. Funct. Mater.* 29 (2019)
28 1904036. <https://doi.org/10.1002/adfm.201904036>.
- 29 [29] H.A. Harwig, A.G. Gerards, Electrical properties of the α , β , γ , and δ phases of bismuth
30 sesquioxide, *J. Solid State Chem.* 26 (1978) 265–274. [https://doi.org/10.1016/0022-4596\(78\)90161-5](https://doi.org/10.1016/0022-4596(78)90161-5).
31
- 32 [30] N.M. Sammes, G.A. Tompsett, H. Näfe, F. Aldinger, Bismuth based oxide electrolytes— structure
33 and ionic conductivity, *J. Eur. Ceram. Soc.* 19 (1999) 1801–1826. <https://doi.org/10.1016/S0955->

1 2219(99)00009-6.

2 [31] F. Yang, M. Li, L. Li, P. Wu, E. Pradal-Velázquez, D.C. Sinclair, Review: Defect chemistry and
3 electrical properties of sodium bismuth titanate perovskite, *J. Mater. Chem. A.* (2018).
4 <https://doi.org/10.1039/C7TA09245H>.

5 [32] M. Li, M.J. Pietrowski, R.A. De Souza, H. Zhang, I.M. Reaney, S.N. Cook, J.A. Kilner, D.C. Sinclair,
6 A family of oxide ion conductors based on the ferroelectric perovskite $\text{Na}_{0.5}\text{Bi}_{0.5}\text{TiO}_3$, *Nat. Mater.*
7 13 (2014) 31–35. <https://doi.org/10.1038/nmat3782>.

8 [33] J.T.S. Irvine, D.C. Sinclair, A.R. West, Electroceramics: characterization by impedance
9 spectroscopy, *Adv. Mater.* 2 (1990) 132–138. <https://doi.org/10.1002/adma.19900020304>.

10 [34] J. Jamnik, J. Maier, Treatment of the Impedance of Mixed Conductors Equivalent Circuit Model
11 and Explicit Approximate Solutions, *J. Electrochem. Soc.* 146 (1999) 4183–4188.
12 <https://doi.org/10.1149/1.1392611>.

13 [35] V.V. Belousov, Surface ionics: A brief review, *J. Eur. Ceram. Soc.* 27 (2007) 3459–3467.
14 <https://doi.org/10.1016/j.jeurceramsoc.2007.01.014>.

15 [36] Y. Tomura, I. Oikawa, H. Takamura, Oxygen vacancy order-disorder transition at high
16 temperature in Bi-Sr-Fe-based perovskite-type oxides, *Phys. Rev. Mater.* 3 (2019) 125802.
17 <https://doi.org/10.1103/PhysRevMaterials.3.125802>.

18

19

20

21

22

23

24

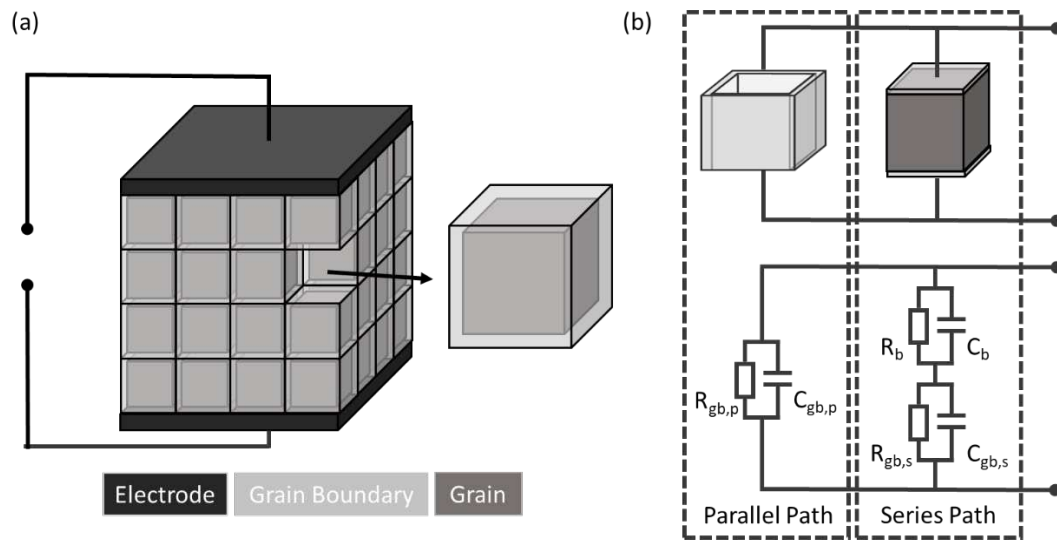
25

26

27

28

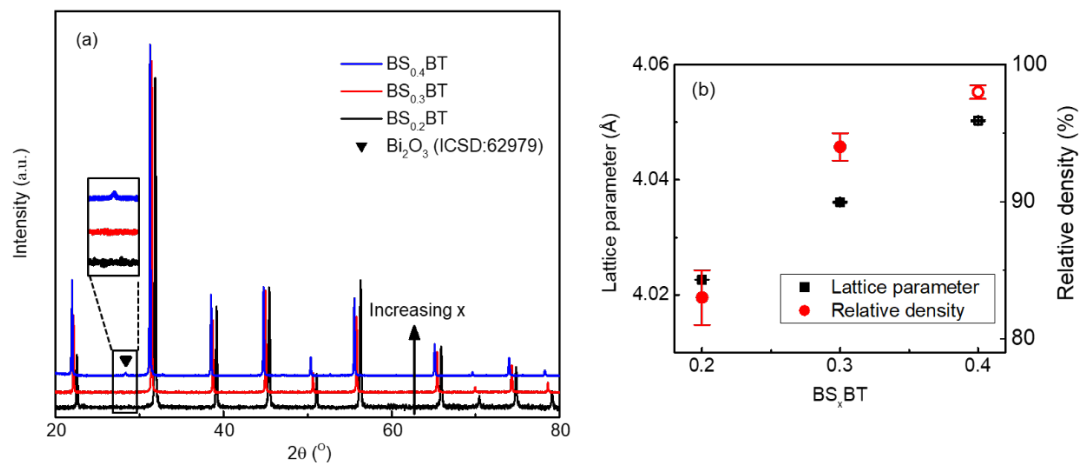
1 Figures



2

3 Figure 1 (a) Schematic of the Brickwork Layer Model (BLM) and (b) generic equivalent circuit
4 associated used for data analysis.

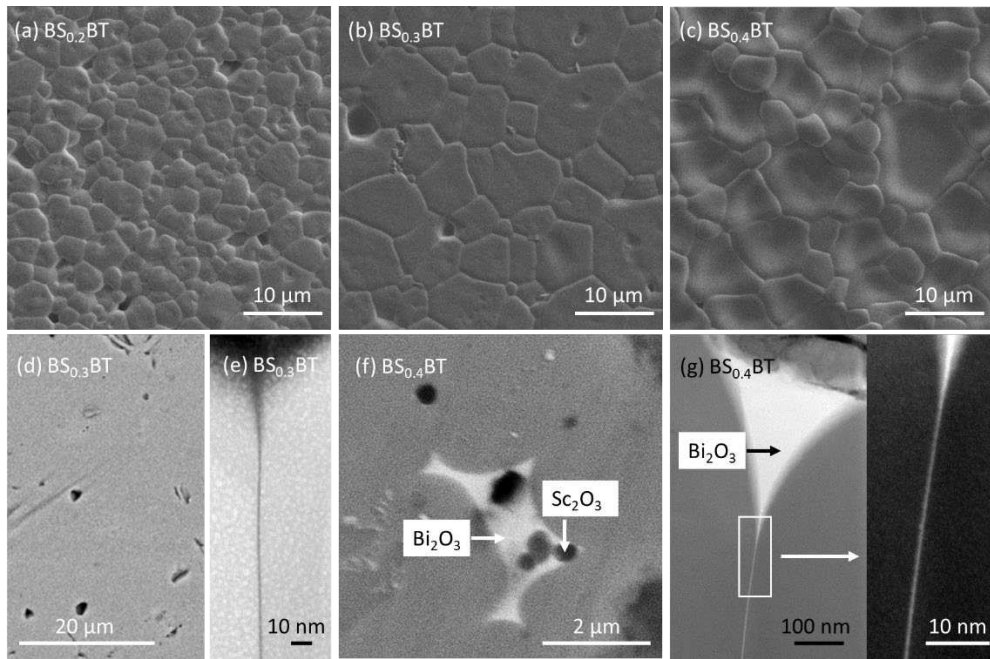
5



6

7 Figure 2. (a) Room temperature X-ray powder diffraction data and (b) lattice parameter and relative
8 density for $x(BiScO_3)-(1-x)(BaTiO_3)$ (BS_xBT) crushed ceramics of $BS_{0.2}BT$, $BS_{0.3}BT$ and $BS_{0.4}BT$.

9



1

2

3

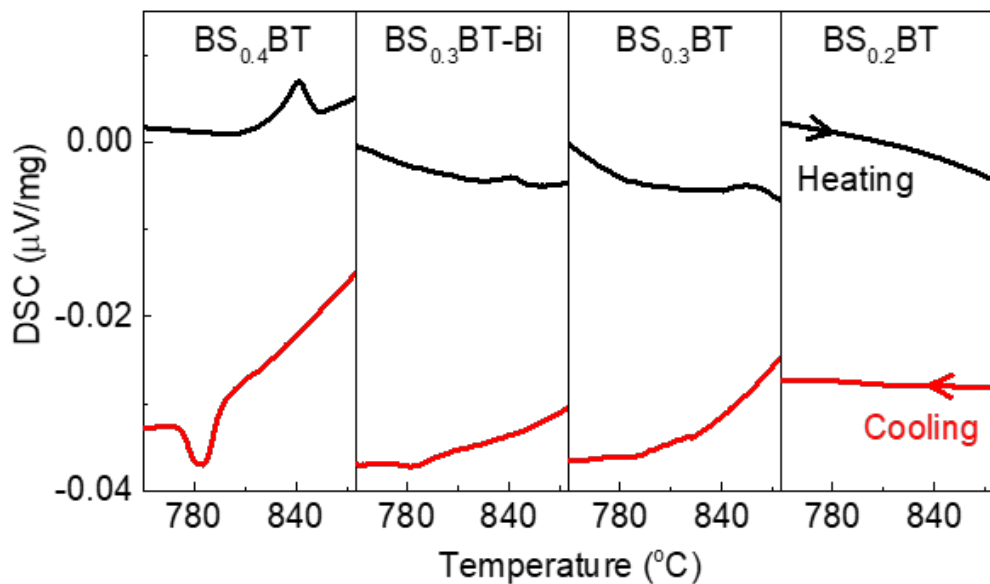
4

5

6

7

Figure 3. SEM secondary electron images of thermal etched $x(\text{BiScO}_3)-(1-x)(\text{BaTiO}_3)$ (BS_xBT) ceramics: (a) $\text{BS}_{0.2}\text{BT}$; (b) $\text{BS}_{0.3}\text{BT}$; (c) $\text{BS}_{0.4}\text{BT}$. SEM back scattered electron images of (d) $\text{BS}_{0.3}\text{BT}$ and (f) $\text{BS}_{0.4}\text{BT}$ showing the presence of Bi rich triple points in only the $\text{BS}_{0.4}\text{BT}$ sample. HAADF-STEM images of a triple pocket and grain boundary in (e) $\text{BS}_{0.3}\text{BT}$ being deficient in atomically heavy Bi relative to the matrix and in (g) $\text{BS}_{0.4}\text{BT}$ being rich in Bi.

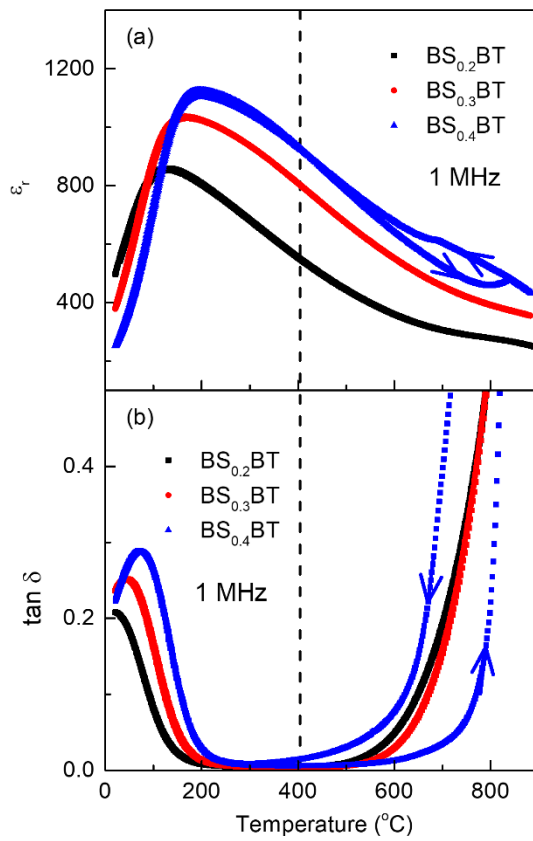


8

9

Figure 4. Differential scanning calorimetry results for selected $x(\text{BiScO}_3)-(1-x)(\text{BaTiO}_3)$ (BS_xBT)

1 samples on a heating and cooling cycle in the range $\sim 750 - 880$ °C.

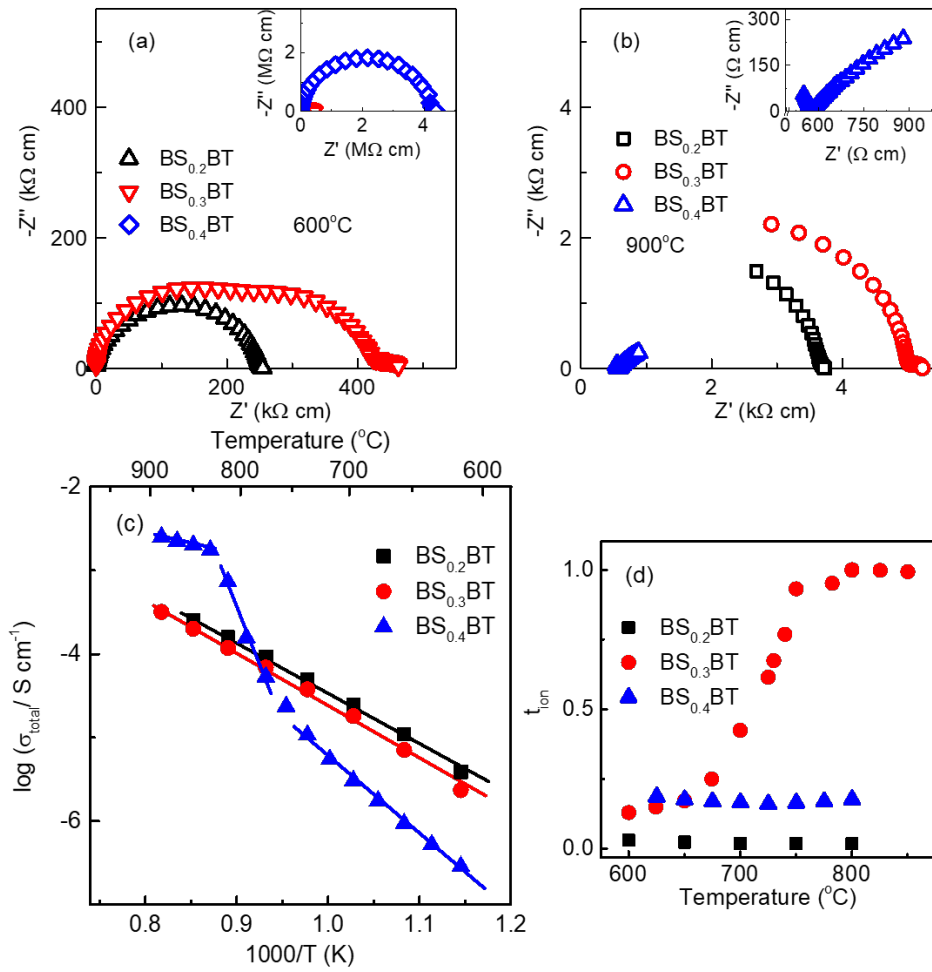


2

3 Figure 5. Temperature dependent (a) ϵ_r and (b) $\tan \delta$ (both at 1 MHz) for $x(\text{BiScO}_3)-(1-x)(\text{BaTiO}_3)$
4 (BS_xBT) ceramics.

5 .

6



1

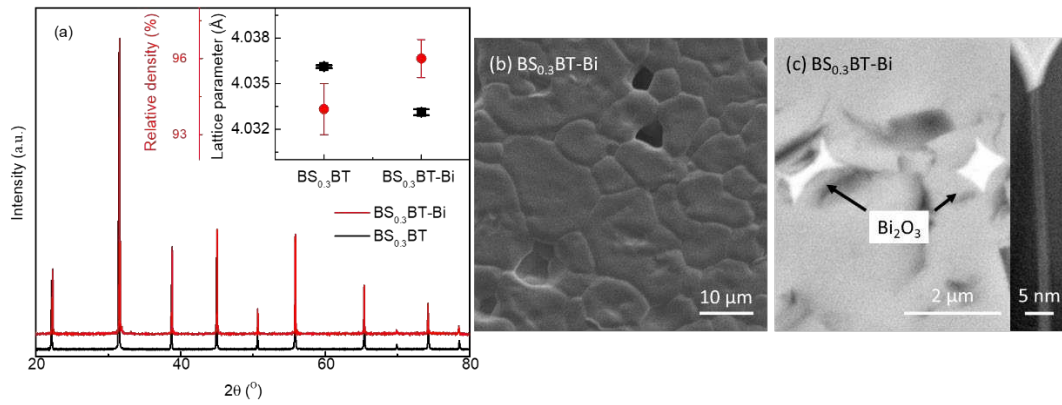
2 Figure 6. Z^* plot of $x(\text{BiScO}_3)-(1-x)(\text{BaTiO}_3)$ (BS_xBT) ceramics at (a) 600°C and (b) 900°C . (c)
 3 Arrhenius plot of total conductivity, σ_T , versus reciprocal temperature and (d) oxide ion transport
 4 number, t_{ion} , of BS_xBT samples.

5

6

7

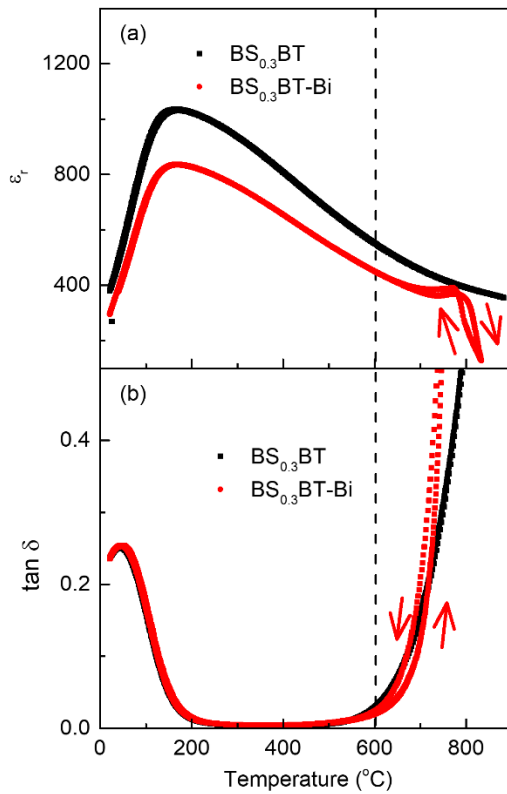
8



1

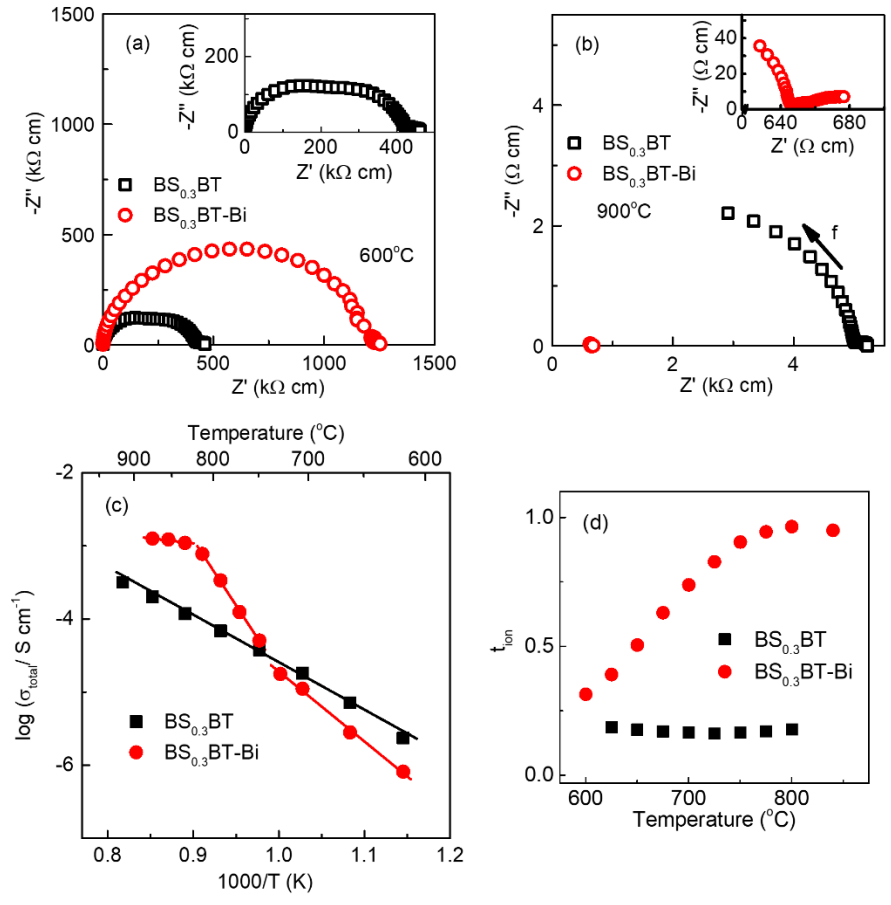
2 Figure 7. (a) Room temperature X-ray powder diffraction data, (b) SEM secondary electron
 3 images of thermal etched and (c) SEM back scattered electron image showing Bi-rich triple points
 4 & HAADF STEM image (on right) showing Bi-rich grain boundaries of $\text{BS}_{0.3}\text{BT-Bi}$ ceramic, i.e.
 5 $0.3(\text{BiScO}_3)\text{-}0.7(\text{BaTiO}_3)$ with 3wt% excess Bi_2O_3 in the starting formulation.

6



7

8 Figure 8. Temperature dependent (a) ϵ_r and (b) $\tan \delta$ (both at 1 MHz) for $\text{BS}_{0.3}\text{BT}$ and $\text{BS}_{0.3}\text{BT-Bi}$, i.e.
 9 $0.3(\text{BiScO}_3)\text{-}0.7(\text{BaTiO}_3)$ without and with 3wt% excess Bi_2O_3 in the starting formulation.



1

2 Figure 9. Z* plot of BS_{0.3}BT and BS_{0.3}BT-Bi ceramics, i.e. 0.3(BiScO₃)-0.7(BaTiO₃) without and with
 3 3wt% excess Bi₂O₃ in the starting formulation, at (a) 600 °C and (b) 900 °C. (c) Arrhenius plot of
 4 total conductivity, σ_T, versus reciprocal temperature and (d) oxide ion transport number, t_{ion}, for
 5 BS_{0.3}BT and BS_{0.3}BT-Bi ceramics.